Cover sheet for 'Response of atmospheric convection to surface drying: new insights from isentropic analysis'

Author 1: Laurel Régibeau-Rockett (Stanford University and National Research Council, laurelregibeau@gmail.com)

Author 2: Morgan O'Neill (University of Toronto, morgan.oneill@utoronto.ca)

Response of atmospheric convection to surface drying: new insights from isentropic analysis

Laurel Régibeau-Rockett[a,b] and Morgan E O'Neill[c]

[a] *Department of Earth System Science, Stanford University, Stanford, California, USA*

[b] *National Research Council, Monterey, California, USA*

[c] *Department of Physics, University of Toronto, Toronto, Canada*

Corresponding author: Laurel Régibeau-Rockett, laurelregibeau@gmail.com

ABSTRACT: There is strong evidence that the atmospheric moisture content of several solar system planets, including Earth, has varied over their lifetimes. A growing body of work also documents a range of atmospheric water vapor content on exoplanets. An improved understanding of the coupling between atmospheric moisture availability and convection could yield greater intuition about the past and current states of planetary atmospheres, including Earth's atmosphere. In this work, we investigate the changing heat engine behavior of localized radiative-convective equilibrium convection in a suite of moist-to-nearly-dry numerical simulations. Each simulation has a constant surface relative humidity, with values ranging from saturated to nearly dry surface conditions. We observe a deepening of the planetary boundary layer and a corresponding lifting of the cloud base as the surface dries, in agreement with previous numerical and observational studies. The primary factor contributing to this is the reduction in the temperature of the lifting condensation level implied by the Clausius-Clapeyron relationship. Additionally, the mass transport by atmospheric convection increases in drier conditions, consistent with prior work. Finally, inspection of the atmospheric circulation in the typical temperature-entropy space used for heat engine analysis implies that the temperature of convective tops is invariant under surface drying, although this result is sensitive to the planetary boundary layer parameterization. This could support the generalization of the Fixed Anvil Temperature hypothesis, which proposes that cloud top temperatures are constant as the surface temperature changes, to convection under varied surface humidity.

1. Introduction

It has long been accepted that moisture is an essential aspect of atmospheric convection on Earth. Compared to a dry atmosphere, for example, a moist atmosphere contains more intense updrafts due to latent heat release, and has narrower convective updrafts compared to the downwelling area. More recent work has demonstrated the far-reaching extent of atmospheric moisture's impacts on convection: Pauluis and Held (2002a) and Pauluis (2011) argued the atmosphere acts both as a heat engine that converts the atmosphere's differential heating into convective motions and as a dehumidifier. These two aspects of atmospheric convection are in competition with each other, with the atmosphere's action as a dehumidifier dominating over its behavior as a heat engine in an idealized moist atmosphere comparable to our own (Pauluis and Held 2002a). This contradicts the assumed dominance of the atmosphere's dry heat engine behavior in previous theories of moist convection (Rennó and Ingersoll 1996; Emanuel and Bister 1996).

The amount of moisture in our atmosphere has likely varied significantly over Earth's lifetime. For example, the Snowball Earth hypothesis posits that during the coldest portions of Earth's lifetime—particularly during subsets of the Neoproterozoic Era (1000–538.8 million years ago)—the Earth's surface was covered by an extensive layer of ice (e.g. Kirschvink 1992; Hoffman et al. 1998; Evans et al. 1997). Such an ice-covered surface would imply a low atmospheric moisture content (though it would also likely be close to saturation, unlike today's highly subsaturated atmosphere). Beyond Earth, mounting evidence suggests that moist convection may be important to the past and current evolution of solar system atmospheres, such as Venus (Kasting 1988), Mars (e.g. Wordsworth et al. 2013; Urata and Toon 2013), and Saturn (Li and Ingersoll 2015). Recent observations of exoplanets have also found significant levels of atmospheric water vapor (e.g. Tsiaras et al. 2019; Benneke et al. 2019; Roy et al. 2023; Mikal-Evans et al. 2023; Piaulet-Ghorayeb et al. 2024; Benneke et al. 2024). For example, many recent studies have focused on the atmospheric composition of the exoplanet K2-18b, with most studies in agreement that water vapor represents on the order of 0.01%-10% of its atmosphere by volume (e.g. Tsiaras et al. 2019; Benneke et al. 2019; Madhusudhan et al. 2020; Changeat et al. 2019). The number of observed exoplanets with expected water-containing atmospheres is likely to grow significantly, with several exoplanets considered as candidates for harboring significant water (e.g. Southworth et al. 2017; Cadieux et al. 2022; Piaulet et al. 2023; Cadieux et al. 2024). It seems likely that a large range of water-containing atmospheres exist in our universe, with varying amounts of atmospheric moisture. Understanding the impact of atmospheric moisture content on the characteristics of atmospheric convection could help us better understand the past evolution and present state of an array of different planetary atmospheres in the solar system and beyond—and most importantly, our Earth's atmosphere.

Previous work has demonstrated that more broadly, the atmospheric abundance of a condensable component is important to atmospheric convective characteristics (e.g. Mitchell et al. 2006; Hueso and Sánchez-Lavega 2006; Barth and Rafkin 2007; Pierrehumbert and Ding 2016; Mitchell and Lora 2016; Ding and Pierrehumbert 2016). While this condensable substance is water on Earth, this may not be the case on other planets. For example, Mitchell (2008) demonstrated, using axisymmetric simulations of Titan's atmosphere, that the atmosphere's characteristics are strongly sensitive to the initial supply of methane, which is the condensable component on Titan. The author found that below a threshold amount of initial methane, Titan's atmosphere abruptly shifted into a warmer state with much less precipitation and a shallower, more asymmetric Hadley cell. An investigation of the effect of atmospheric moisture on convective characteristics may have implications for convection in planetary atmospheres containing a condensable component that is not water.

A common idealized framework used to study the behavior of localized atmospheric convection is that of radiative-convective equilibrium (RCE). In the idealized modelling context, the term RCE refers to the statistically steady state of an idealized simulated atmosphere that experiences both net radiative cooling and surface heating. To date, only a few studies have examined the changes in atmospheric behavior between moist and dry RCE. Pauluis and Held (2002a,b) compared the characteristics of convection between moist and dry RCE in a cloud permitting model (CPM) using an entropy budget. In addition, both Mrowiec et al. (2011) and Wang and Lin (2020, 2021) studied differences in the properties of tropical cyclones between moist and dry RCE frameworks. A comparison of the characteristics of moist and dry RCE convection was also performed by Singh and O'Neill (2022).

Only a few studies have investigated the moist-to-dry transition itself. First, Pauluis (2000) performed an entropy budget of moist-to-dry RCE convection in a CPM. The author found that from an energetic perspective, atmospheric convection retains moist behavior for the majority of the moist-to-dry transition, until the atmospheric moisture content has decreased by roughly

90%. This moist regime is characterized by the dominance of the energetic consumption of moist processes over the kinetic energy of convective motions and a greater portion of the total mechanical work dissipation occurring in shear zones surrounding falling hydrometeors rather than via the turbulent cascade. Later, Alland et al. (2017) investigated the impact of midlevel dry-air entrainment on tropical cyclones by applying Pauluis and Mrowiec (2013)'s technique of isentropic analysis to a suite of CPM ensembles initialized with different levels of atmospheric moisture. The ensembles initially had the same sea surface temperature and an identical subcloud vapor mixing ratio, but had different values of the initial moist entropy deficit above this point. The authors found no significant differences in the impacts of mid-level entrainment on the entropy of the eyewall updraft under atmospheric drying. However, the convective mass transport of the overturning circulation decreased under atmospheric drying, implying that dry mid-level air may impact the tropical cyclone circulation via entrainment into the inflow layer. Another study by Zsom et al. (2012) developed and studied a 1D microphysical cloud model for planets in the habitable zone. Using Earth-like model parameters, the authors reduced the atmospheric relative humidity from 100% to 20% across a suite of simulations[1]. They found that liquid water clouds formed at higher altitudes as the atmospheric relative humidity decreased, whereas the altitude of ice cloud formation was largely insensitive to the relative humidity. Finally, Cronin and Chavas (2019) investigated the moist-to-dry transition of atmospheric convection for the specific case of tropical cyclones. The authors found that their simulated tropical cyclones exhibited a more gradual transition from moist to dry characteristics compared to the findings of Pauluis (2000), although it should be noted that no tropical cyclones formed for their simulations with mid-to-low values of atmospheric moisture.

Some key differences exist between these moist-to-dry studies of Pauluis (2000) and Cronin and Chavas (2019), which could explain the contrast in the sharpness of the transition from moist to dry atmospheric behavior found in these works. First, whereas Pauluis (2000) investigated the moist-to-dry behavior of disorganized atmospheric convection, Cronin and Chavas (2019) studied tropical cyclones, which are highly organized systems. Organized convective systems may experience the moist-to-dry transition quite differently from localized convection. Second, Pauluis (2000) examined the moist-to-dry transition from the perspective of the atmosphere's behavior as a heat engine, with a focus on its changing energetics, whereas Cronin and Chavas (2019) examined changes in more "classical" tropical cyclone characteristics including the tropical

[1]The authors also ran simulations with relative humidity values lower than 20%, but these exhibited unphysical behavior and so were discarded.

cyclone intensity and radius of maximum winds. Viewing atmospheric systems in terms of their thermodynamic behavior as heat engines, rather than in terms of these classical characteristics, could yield a different view on the changes in behavior of such systems over the transition. Finally, the construction of the moist-to-dry transition was different in these two studies. Whereas Cronin and Chavas (2019) varied the surface saturation specific humidity in their simulations, Pauluis (2000) varied the saturation specific humidity of the whole atmosphere. Such differences in the construction of the transition may have large impacts on the changing behavior of convection. For example, as noted by Pauluis (2000), his construction of the moist-to-dry transition results in hydrometeor fall velocities remaining at the same order of magnitude regardless of the reduction in hydrometeor water mass. This may have a strong impact on the variability of atmospheric cloud content as the atmosphere dries, resulting in an artificially steep decrease in cloud amounts. This could significantly affect the variability of atmospheric convection over the transition.

Pauluis and Mrowiec (2013) developed the procedure of "isentropic analysis". Isentropic analysis supports the computation of an alternative streamfunction of the atmospheric circulation cast into height and equivalent potential temperature space. This space has greater relevance to the thermodynamic behavior of the atmospheric heat engine compared to the classical Eulerian space in which convective streamfunctions are typically constructed. Several previous works have employed isentropic analysis to study the behavior of atmospheric convection and convective systems in different contexts (e.g. Singh and O'Gorman 2015; Pauluis 2016; Mrowiec et al. 2016; Muller and Romps 2018; O'Neill and Chavas 2020; Li et al. 2023; Régibeau-Rockett et al. 2024). For example, some studies have employed a version of isentropic averaging developed for tropical cyclones (Mrowiec et al. 2016) to study the impacts of drying above the lifting condensation level on the secondary circulation of tropical cyclones (Alland et al. 2017), the evolution of tropical cyclones from an energetic perspective (Fang et al. 2019; Li et al. 2023), and tropical cyclone energetics in the mature state (Pauluis and Zhang 2017). Isentropic averaging has also been applied to both localized atmospheric convection (e.g. Pauluis and Mrowiec 2013; Pauluis 2016) and to organized convective systems (e.g. Mrowiec et al. 2015; Dauhut et al. 2017) to yield new understanding on the behavior of these systems. For example, Pauluis (2016) found that a doubling of the atmospheric carbon dioxide concentration results in a larger convective entropy transport. This results in an increase in the total energy production by the convective heat engine, although the partitioning of this energy between moist processes and the kinetic energy of convective motions does not significantly change.

In this study, we apply isentropic analysis to a suite of RCE CPM simulations with varying levels of surface moisture, where the moisture transition is constructed by varying the surface saturation mixing ratio following Cronin and Chavas (2019). The goal of this analysis is to investigate how the thermodynamic behavior of localized convection varies as the available surface moisture decreases from fully moist conditions, without rotation. The paper is structured as follows: in section 2 we describe our suite of simulations and the analysis methodology, including a summary of the isentropic analysis method. In section 3, we present the results of our analyses. Finally, in section 4 we provide a discussion of our results and present some conclusions.

2. Methods

a. Model description

In this work, we analyze changes in atmospheric behavior in a suite of moist-to-near-dry simulations conducted using the Cloud Model 1 (CM1, Bryan and Fritsch 2002), version 21.1. In general, the design of our simulations emulates Singh and O'Gorman (2016), who performed an entropy budget on a suite of simulations over different sea surface temperatures in CM1 version 16 with added alterations. Their modifications to CM1 and the design of their suite of simulations had the goal of conserving energy and mass well enough that their entropy budget could be closed within an acceptable margin of error. Although we do not perform an entropy budget in our work, we adopt a similar simulation design with the goal of improving the model's conservation of energy and mass.

All simulations are in a non-rotating 84 km $\times$ 84 km doubly-periodic domain. This domain size is smaller than the 200-300 km domain size required to support self-aggregation (Muller and Held 2012; Jeevanjee and Romps 2013). The domain has a 1-km horizontal grid spacing and a vertically stretched grid spacing (Wilhelmson and Chen 1982) ranging from 50 m at a height of 0 km to 500 m from 5.5 km up to the model top at 27 km. A Rayleigh damping layer is imposed in the top 3 km. The simulations are run with CM1's mesoscale modelling setup and the Yonsei University (YSU) planetary boundary layer parameterization (Hong et al. 2006). Microphysics is parameterized using the Morrison six-species double-moment scheme (Morrison et al. 2005,

2009) with hail as the large ice category. The radiation scheme is the RRTMG interactive scheme. Following Bretherton et al. (2005), we remove the diurnal and seasonal cycles from the radiative scheme via fixing the solar constant at 650.83 W m^{-2} and the solar zenith angle at 50.5°. We employ a Smagorinsky parameterization scheme for horizontal turbulence (Bryan and Rotunno 2009), a sixth-order hyper-diffusion scheme, and a sixth-order nondiffusive advection scheme. As in Singh and O'Gorman (2016), the sea surface temperature is set to 301.5 K. The simulations include dissipative heating and employ a set of equations for the moist microphysics that improves the conservation of energy and mass by accounting for the heat capacity of hydrometeors (Bryan and Fritsch 2002) and including the vertical transport of energy associated with hydrometeor sedimentation.

The surface layer in our simulations is parameterized following the Weather Research and Forecasting model (WRF, Skamarock et al. 2008) MM5 scheme (Grell et al. 1994), as modified by Jiménez et al. (2012). We varied the surface dryness in our simulations by adding a scaling factor β to the surface saturation mixing ratio in the latent heat flux formula of the surface layer model in a similar manner to Cronin and Chavas (2019):

$$LHF = \rho_1 L_{v,s} C_q U(\beta r_s^* - r_{v,1}). \tag{1}$$

Here, ρ_1 (kg m^{-3}) and $r_{v,1}$ (kg kg^{-1}) are the dry-air density and water vapor mixing ratio, respectively, in the surface layer (Jiménez et al. 2012). In CM1, this corresponds to the lowest model level of 25 m. U is the horizontal wind speed (m s^{-1}) at 10 m enhanced by a convective velocity as in Beljaars (1995) and a subgrid velocity following Mahrt and Sun (1995), r_s^* (kg kg^{-1}) is the saturation water vapor mixing ratio at the surface, and C_q is the dimensionless bulk transfer coefficient. The term $L_{v,s}$ (J kg^{-1}) is the latent heat of vaporization at the surface, defined as:

$$L_{v,s} = L_{v,0} + (c_{p,v} - c_{p,l})(T_s - T_{ref}),$$

where T_s (K) is the surface temperature, $L_{v,0}$ (J kg^{-1}) is the latent heat of vaporization at a reference temperature T_{ref} of 273.15 K, and $c_{p,v}$ and $c_{p,l}$ are, respectively, the specific heat capacities (J kg^{-1} K^{-1}) of water vapor and liquid water.

The term β in Eq. (1) is a dimensionless constant and controls the amount of available moisture that can exit the surface. A value of 1 corresponds to a typical surface moisture supply given the sea surface temperature of 301.5 K (i.e., a saturated or “fully moist” surface), whereas a value of 0 is equivalent to a surface with no available moisture to evaporate into the atmosphere (i.e., an effectively “fully dry” surface). In this way, β can be thought of as the surface relative humidity. We vary the value of the β parameter from 1 to 0.1 over the suite of simulations, which allows us to investigate the impacts of surface drying on localized RCE convection. We choose to examine a range of β values from 1 to no lower than 0.1 because simulations with lower values of β did not achieve an RCE state within an 100-day time frame.

The simulations are initialized with no initial perturbation and vertical profiles of potential temperature and moisture computed from a period of 10 statistically steady days from the end of RCE simulations with an identical design, but that are initialized with the Dunion (2011) moist tropical sounding. A similar initialization method was used in the moist-to-dry simulations of Cronin and Chavas (2019). The initialization simulations have a model top of 28 km, 1 km higher than the domain height of the main suite of simulations. This is due to CM1’s requirement that input soundings must extend higher than the chosen model top. The upper-level Rayleigh damping layer thickness in these simulations matches that of the main set of simulations, and so the damping layer begins 1 km higher in the initialization simulations.

A total of five simulations are conducted, with β set to 1, 0.75, 0.5, 0.25, and 0.1. Following initialization simulations lasting between 32 and 83 days, with the time to RCE increasing as β decreased, the simulations reached a statistical equilibrium after approximately 50 days (Fig. 1). This RCE state was identified following the procedure described in Text S1 of the online supplemental materials. The presence of a statistically steady state after the point where RCE is first identified is confirmed by visual inspection of Hovmöller diagrams, constructed with daily data, of the vertical profile of equivalent potential temperature (θ_e) in each simulation (Fig. 1). In this work, θ_e is defined as in Bryan (2008):

$$\theta_e = T(\frac{p_{ref}}{p_d})^{\frac{R_d}{c_{p,d}}} \mathscr{H}^{-\frac{r_v R_v}{c_{p,d}}} \exp\left[\frac{r_v L_{v,0}}{c_{p,d} T}\right],$$

where T is the temperature (K), p_{ref} = 1000 hPa is the reference pressure, p_d is the partial pressure of dry air (hPa), R_d ais the gas constant for dry air, $c_{p,d}$ (J kg^{-1}K^{-1}) is the specific heat

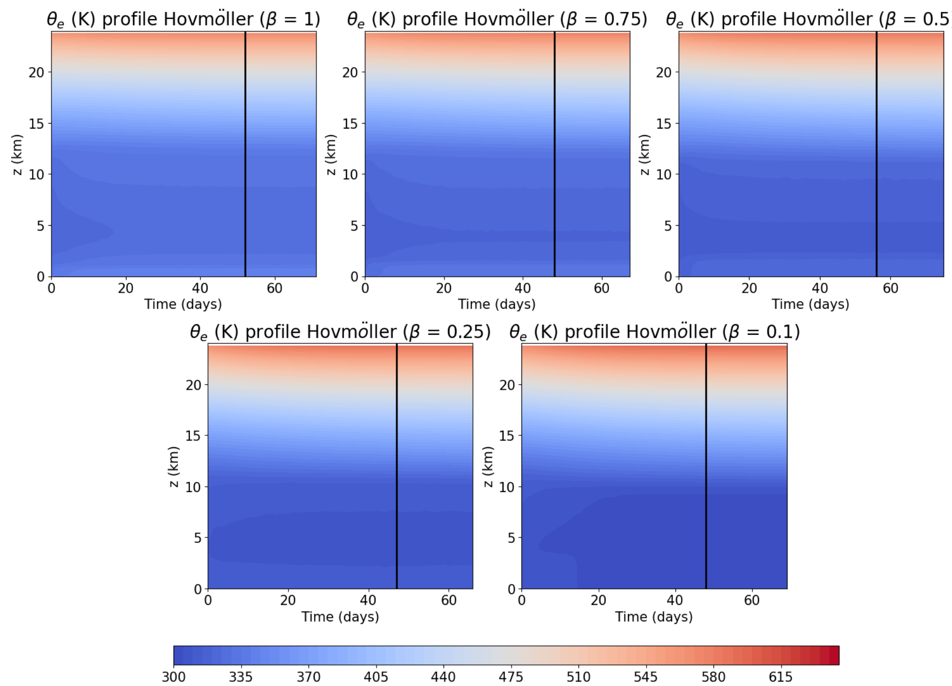

FIG. 1. Hovmöller plots of the time- and horizontal-mean vertical profiles of equivalent potential temperature (colors) in each constant-β simulation. Values from within the model sponge layer are not shown. The black vertical line denotes the start of the 20-day steady-state period that we analyze for each simulation.

capacity of dry air, r_v is the water vapor mixing ratio (kg kg^{-1}), and $\mathscr{H}$ is the relative humidity with respect to liquid water:

$$\mathscr{H} = \frac{e_p}{e_s},$$

where e_p is the water vapor pressure (Pa) and e_s (Pa) is the saturation vapor pressure of Bolton (1980).

Once statistical equilibrium was achieved, we ran the simulations for a further 20 days with output data every 4 hours. The beginning of each of these 20-day periods is denoted by the vertical black lines in Fig. 1. In what follows, we apply isentropic analysis to these 20-day periods, as will be described in section 2b.

b. A Summary of Isentropic Analysis

In this work, we apply the isentropic analysis procedure to 20-day steady-state periods from each of the simulations described above. In our work, isentropic analysis is broken into the following steps (Pauluis 2016):

1. Compute the isentropic-average[2] vertical mass flux $\langle \rho w \rangle(z, \theta_e)$ (kg m^{-2} s^{-1} K^{-1}) following Eq. (1) of Pauluis and Mrowiec (2013). $\langle \rho w \rangle$ is the time- and horizontal-average of the vertical mass flux at a given height z that was binned by the corresponding equivalent potential temperature value θ_e.

2. Use $\langle \rho w \rangle$ to compute the isentropic streamfunction $\psi(z, \theta_e)$ (Fig. 2) following Eq. (3) of Pauluis and Mrowiec (2013). For given values of z and θ_e, $\psi(z, \theta_e)$ is the cumulative isentropic-average upward mass flux for equivalent potential temperature values less than or equal to θ_e.

3. Use the isentropic streamfunction to construct a set of representative thermodynamic trajectories. When plotted as a contour plot with N levels, $\psi(z, \theta_e)$ is represented as a set of closed loops in $z - \theta_e$ space (Fig. 2). The isentropic analysis method implicitly assumes that these closed loops represent the mean trajectories of real air parcels in the atmospheric system. This assumption was shown to hold reasonably well in the context of axisymmetric tropical cyclones in Régibeau-Rockett et al. (2024).

4. Compute the mass-weighted isentropic-average values of thermodynamic quantities f, such as the absolute temperature and moist entropy: $\tilde{f} = \langle \rho f \rangle / \langle \rho \rangle$.

5. Interpolate these mass-weighted isentropic-average thermodynamic quantities $\tilde{f}$ onto the constructed trajectories. The result is a projection of the isentropic streamfunction into different thermodynamic spaces, such as temperature-entropy space. Projecting the isentropic streamfunction into different spaces in this way can provide a new perspective on the influence of environmental changes on the atmospheric convection.

---

[2] Although the standard nomenclature for this and other procedures involved in isentropic analysis uses the term "isentropic", these computations do not involve constant-entropy conditions.

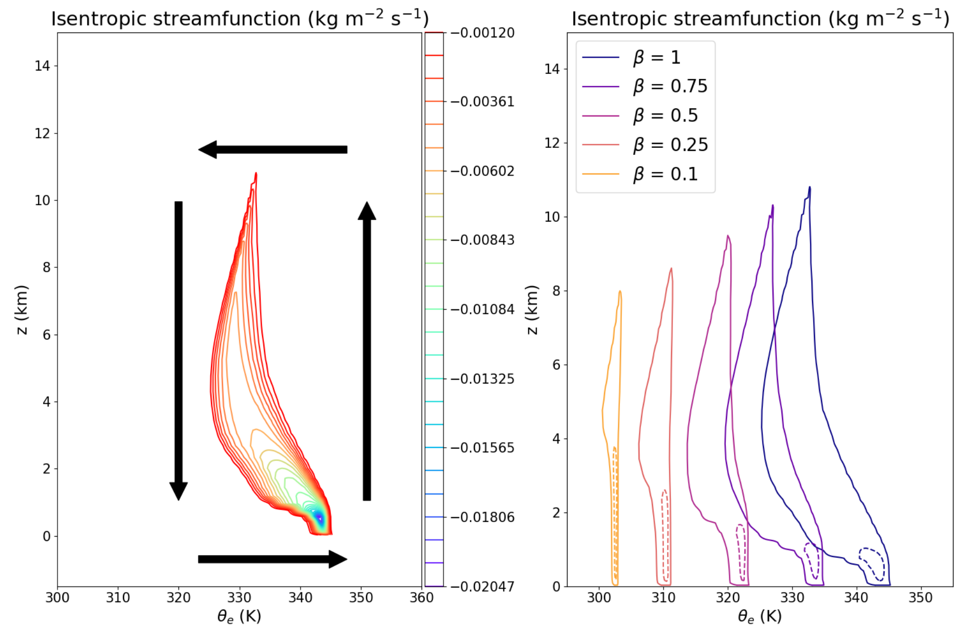

FIG. 2. Left: Isentropic streamfunction, $\psi(z, \theta_e)$, obtained from the 20-day steady state period of the β = 1 simulation. Black arrows show the direction of the thermally direct overturning circulation in $z-\theta_e$ space. Right: Comparison of the deepest trajectories (solid lines) derived from ψ during the 20-day steady-state period of each simulation. Also shown are the median trajectories (dashed lines).

3. Results

In this section, we present the results of applying the isentropic analysis to 20-day steady-state periods from each of the constant-β simulations. We begin by presenting the transition of the atmospheric circulation in response to surface drying viewed in terms of the isentropic streamfunction. This streamfunction is then projected into different thermodynamic spaces, which yields additional insight on the changing behavior of the atmospheric circulation over the transition.

Because our work investigates the impact of the atmospheric moisture content on convective dynamics, our results may be sensitive to our choice of microphysical scheme. We checked the sensitivity of our results to the microphysics parameterization by running two suites of simulations identical to those discussed in section 2, but that had different representations of microphysics: the first suite employed the Thompson microphysics scheme (Thompson et al. 2008; Thompson and Eidhammer 2014), whereas the second used the double-moment graupel-and-hail NSSL microphysics parameterization (Ziegler 1985; Mansell et al. 2010; Mansell and Ziegler 2010). We also examined the sensitivity of our results to the planetary boundary layer (PBL) parameterization in two suites of sensitivity simulations. The first suite used the Mellor-Yamada-Nakanishi-Niino (MYNN) level 2.5 PBL scheme (Nakanishi and Niino 2006, 2009; Olson et al. 2019), while the second used the NCEP Global Forecast System scheme (GFS-EDMF, Hong and Pan 1996). More information on these sensitivity tests, together with the results of analyzing these four simulation suites, can be found in Texts S2 and S3. In general, we find that the results presented in this section are not sensitive to the microphysical or PBL schemes. Henceforth, we will note instances where our results are qualitatively sensitive to these parameterizations.

a. Effects of Moisture on the Isentropic Streamfunction

Figure 2 presents changes in selected trajectories from the isentropic streamfunction over the suite of simulations. We show here changes in both the deepest trajectory and a median trajectory, defined as the twelfth of 25 levels used to plot ψ in step 3 of the isentropic averaging process described in section 2b. The changes in the isentropic streamfunction reveal changes in the characteristics of the atmospheric circulation: first, as the surface dries, the depth of the circulation decreases. In addition, the range of equivalent potential temperatures sampled by the circulation decreases, with more similar values of θ_e for updrafts and downwelling air. This is unsurprising, since a smaller difference in θ_e between rising and sinking air is characteristic of dry convection. As β decreases, we also observe an increase in the depth of the atmospheric boundary layer, or equivalently an increase in the lifting condensation level (LCL). In Fig. 2, the LCL is the level at which the θ_e range of the isentropic circulation noticeably increases, with the PBL below represented by the region in which rising air has a similar equivalent potential temperature value as sinking air. This is because the LCL is the level at which latent heat begins to be released by rising air parcels.

We next study the variability of the isentropic mass circulation, $\Delta\psi$ (kg m^{-2} s^{-1}). The quantity $\Delta\psi$ is the mass circulation in each of the N levels of the isentropic streamfunction, defined following Pauluis (2016) as $\Delta\psi = -N^{-1}\psi_{min}$, where ψ_{min} is the minimum value of ψ. By construction, this is the same for each level of the isentropic streamfunction. As can be seen in Fig. 3, $\Delta\psi$ increases by 80% between the fully moist and driest simulations. Note that the percentage change in mass circulation is computed with respect to its value in the fully moist simulation. Because $\Delta\psi$ represents the mass transport of each level of the isentropic streamfunction, with high-θ_e air

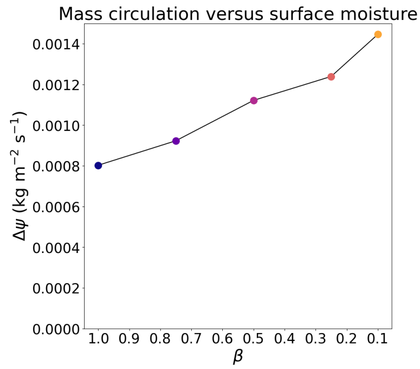

FIG. 3. Isentropic mass circulation $\Delta\psi$, computed during the 20-day steady-state periods from each simulation, versus β.

rising and low-θ_e air sinking, the increase in $\Delta\psi$ should indicate an increase in the convective heat transport. However, in our simulations, the radiative cooling rate and total surface heat flux in the domain, computed as described in the appendix, decrease strongly as the surface dries (Fig. 4). In RCE, these quantities are balanced by the convective heat transport, implying that the heat transport also decreases as the atmosphere dries. This is not incompatible with the increase in the convective mass transport because the heat transport is also dependent on the difference in θ_e between the updraft and downwelling air. This difference decreases significantly with decreasing β (Fig. 2), and so acts to decrease the convective heat transport. Overall, the decrease in the updraft/downwelling θ_e difference outweighs the increased convective mass transport in terms of its impact on the convective heat transport, resulting in the lower convective heat transport that we observe under surface drying. It is interesting to note, however, that the decline in the external heating and cooling of the atmosphere under drying is sufficiently slow compared to the narrowing of the updraft-downdraft difference in θ_e that the circulation must intensify to maintain a sufficiently large convective heat transport.

As discussed in Marquet (2017), the isentropic streamfunction may have very different characteristics depending on the definition of the equivalent potential temperature. This may impact the robustness of the subset of our results that depend on the equivalent potential temperature. Given this, we examined changes with surface drying in the deepest and median trajectories from the isentropic streamfunction, with this streamfunction computed using Marquet (2011)'s entropy potential temperature θ_s (Text S4). In agreement with Marquet (2017), the shape of the isen-

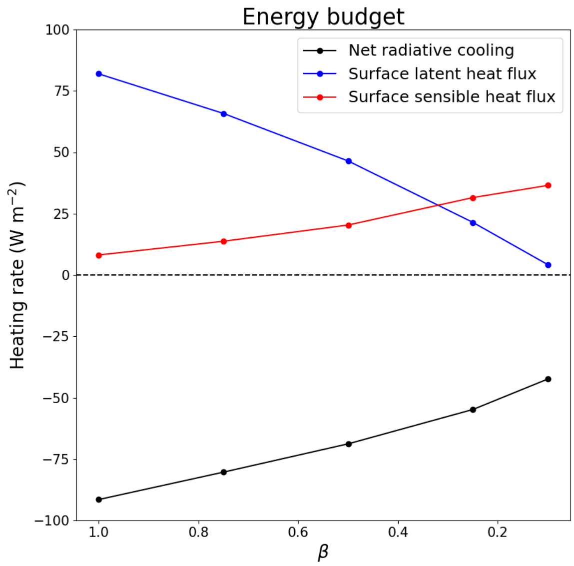

FIG. 4. Time-mean, domain-integrated radiative heating rate divided by the area of the surface (black line), and time- and horizontal-mean surface latent (blue line) and sensible (red line) heat fluxes, computed during the 20-day steady-state periods from each simulation, versus β.

tropic streamfunction is quite different when this alternative coordinate system is used (Fig. S33). However, the trends discussed in this text under surface drying are less qualitatively sensitive to the definition of the equivalent potential temperature. Firstly, the isentropic mass circulation still increases as β decreases (Fig. S34). Otherwise, a minor difference between our main results and those obtained with θ_s is that it is not clear that the difference in the entropy potential temperature between the updraft and the downdraft decreases under surface drying, with the exception of the driest experiment (Fig. S33).

b. Surface Drying Transition in Other Thermodynamic Spaces

Figure 5 presents the response to surface drying of the isentropic streamfunction projected into three thermodynamically-relevant spaces: temperature-entropy (Fig. 5a, b), vapor mixing ratio-vapor Gibbs free energy (Fig. 5c, d), and height-total mixing ratio space (Fig. 5e, f). All quantities are defined as in Régibeau-Rockett et al. (2024). Note that the Gibbs free energy of water vapor g_v can be approximated as $g_v \approx R_v T \log \mathscr{H}$ (Pauluis 2011). The term g_v is primarily dependent on changes in $\mathscr{H}$ (Pauluis 2016), and is close to zero at saturation and negative/positive for unsaturated/supersaturated air. For example, in the simulation with β=1, the unsaturated near-surface air is represented by the portion of the deep trajectory with $g_v \approx -50$ kJ kg^{-1} and the vapor mixing ratio r_v increasing from roughly 0.015 to 0.016 kg kg^{-1} (Fig. 5c). The LCL is the point at which air rising upwards from the surface at relatively constant r_v reaches the point past which g_v is close to zero, representing the saturated updraft. Atmospheric convection involves the removal of water at a higher (near-zero) Gibbs free energy than the value of g_v at which water is added via surface evaporation (Pauluis 2011, 2016). This separation results in irreversible entropy production that reduces the mechanical work output from the atmospheric heat engine (Pauluis 2011, 2016).

The projection of ψ into height-total mixing ratio ($z - r_T$) space (Fig. 5e,f) demonstrates in greater detail the increase in height of the LCL—represented by the height at which the range of the total vapor mixing ratio r_T (kg kg^{-1}) increases markedly between the updraft and the downdraft—over the transition. As can be seen in the temperature-entropy plot (Fig. 5b), the temperature at which the entropy range of the circulation experiences a large growth decreases with increased surface drying. This implies that the temperature of the LCL diminishes with decreasing β. This is in line with Bolton (1980)'s formula for the temperature of the LCL implied by the temperature dependence of the saturation vapor pressure. Specifically, if rising air has a lower vapor mixing ratio, the temperature at which the mixing ratio of the air reaches its saturated value must also be lower. The decrease in the temperature and increase in height of the LCL in response to surface drying is confirmed by inspection of the horizontal- and time-mean vertical profiles of temperature in the simulations (Fig. 6). Here, the LCL is the point above which the lapse rate becomes less negative with height due to the latent heat released in convective updrafts.

The sharp decrease in the updraft entropy of the deep trajectory above the LCL in temperature-entropy space (Fig. 5a) is likely representative of the exchange of water mass between the updraft and its environment due to convective entrainment and detrainment (Pauluis 2016). In tropical cyclones, the eyewall updraft air experiences a very small decrease in the entropy of updraft air due to little dry-air entrainment occurring during ascent (Pauluis and Zhang 2017). For our simulations, the decrease in updraft entropy, Δs_{up}, is much weaker for lower values of β (Fig. 5b), which could represent a decrease in convective entrainment and detrainment. Another possible explanation is that these processes occur, but do not substantially change the entropy of the updraft

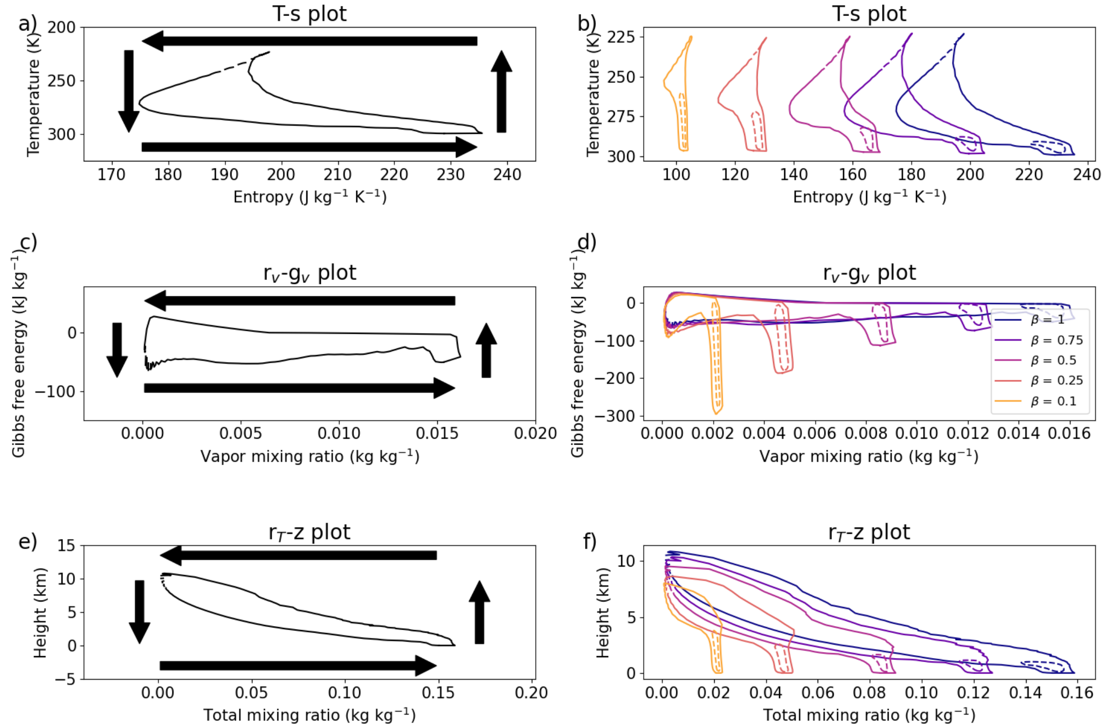

FIG. 5. Left: Isentropic streamfunction, $\psi(z, \theta_e)$, from the $\beta = 1$ simulation projected into a) temperature-entropy space, c) vapor mixing ratio-vapor Gibbs free energy space, and e) height-total water mixing ratio space. Black arrows show the direction of the thermally direct overturning circulation. Right: Comparison of the deepest (solid lines) and median (dashed lines) trajectories derived from ψ for each simulation in b) temperature-entropy space, d) vapor mixing ratio-vapor Gibbs free energy space, and f) height-total water mixing ratio space.

air as consequence of a more uniform atmospheric humidity distribution. Fig. 7 shows the changes in the isentropic-average vapor mixing ratio as the surface dries, together with the deep and median trajectories from the isentropic streamfunction. The humidity gradient between the rising and descending branches of the circulation strongly decreases as β is lowered. This may imply that there is not a reduction of convective entrainment and detrainment as the surface is dried. Instead, these processes likely do not result in a significant modification of the updraft humidity. The absence of significant variability in the humidity during the updraft in the low-β simulations can also be identified in the $z - r_T$ plot (Fig. 5f) of the deepest trajectory, which shows notable fluctuations in the total water mixing ratio during the updraft for the high-β simulations. Such fluctuations are a consequence of the combined processes of entrainment and detrainment

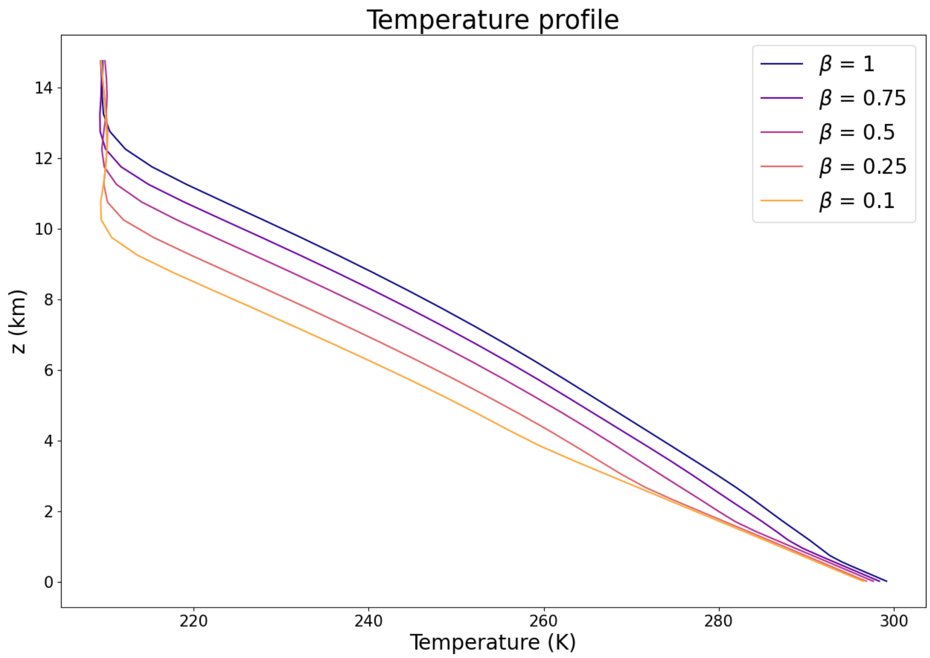

Fig. 6. Time- and horizontal-mean vertical profiles of absolute temperature (K) from the 20-day steady-state periods in each constant-β simulation.

in atmospheres with high contrasts between the humidity of the downdraft and updraft, and are absent in the drier simulations[3].

As in section 3a, we verify the robustness of this decrease in the magnitude of Δs_{up} under surface drying using Marquet (2011)'s moist entropy. We find that as with our isentropic streamfunction results, the shapes of the temperature-entropy diagrams are quite different when this alternative definition of the entropy is employed—with, for example, Marquet (2011)'s entropy increasing during the updraft (Fig. S33), in contrast to the updraft decrease seen in Pauluis (2016)'s moist entropy, which we use in our work (Fig. 5a,b). The different signs of Δs_{up} for these two definitions of the entropy may reflect the sensitivity of each to different diabatic processes: Pauluis (2016)'s moist entropy is only weakly sensitive to the addition or removal of liquid water from an air parcel, whereas Marquet (2011)'s entropy is more sensitive to such processes. However, despite the

[3]The absence of these fluctuations in low-β compared to high-β simulations is also found in both of our other microphysics suites, but this contrast is weaker for the suite with Thompson microphysics (Text S2).

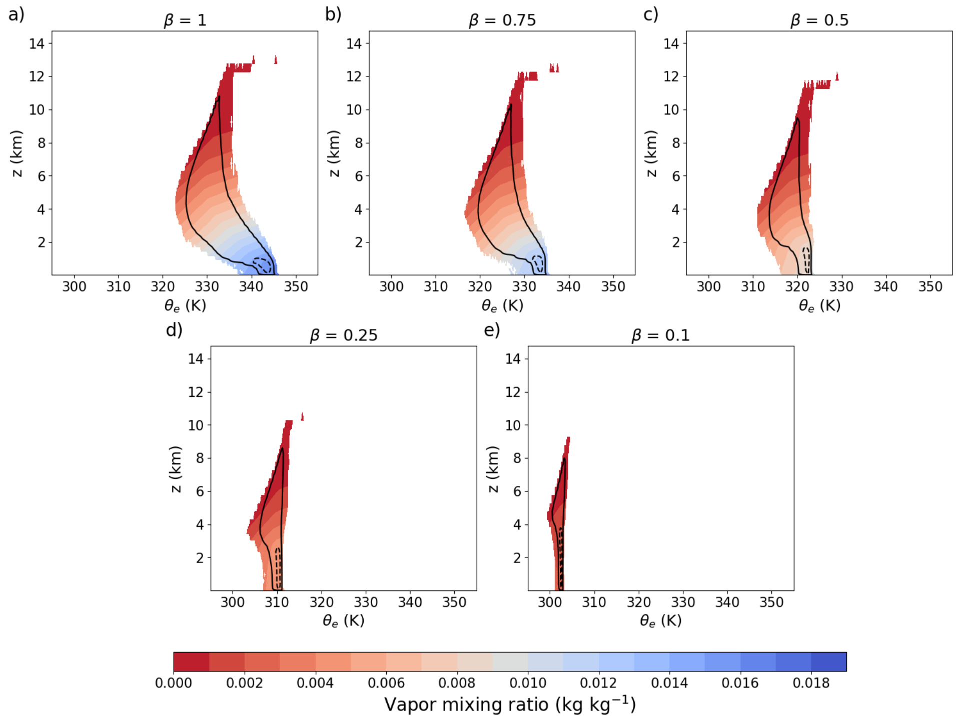

FIG. 7. Comparison of the mass-weighted isentropic-average vapor mixing ratio (colors), and the deepest and median trajectories from ψ for the simulations with β = a) 1, b) 0.75, c) 0.5, d) 0.25, and e) 0.1. All quantities are computed during the 20-day steady-state periods from each simulation.

different shapes of the two temperature-entropy diagrams, the magnitude of Δs_{up} still decreases as the surface dries in both cases.

The smaller decrease of r_T during the upward branch of the deep trajectory in $z - r_T$ space implies a lower precipitation rate in the drier simulations (Fig. 5f). This is confirmed by inspection of the time- and horizontal-average surface precipitation rate in the constant-β simulations (Fig. 8), which decreases by 95% from the fully moist simulation to the simulation in which $\beta = 0.1$.

Over the transition from moist to nearly dry, the change in g_v between the surface and the updraft increases by about a factor of six (Fig. 5d). As the relative humidity of the surface—the source of moisture to the atmosphere—decreases, the irreversibility associated with surface evaporation grows significantly, represented by the increasingly low value of g_v near the surface.

Although the surface value of g_v varies over the simulations, its value for the upper regions of the circulation—recognizable as the portion of the deep $r_v - g_v$ trajectory with r_v below 0.001

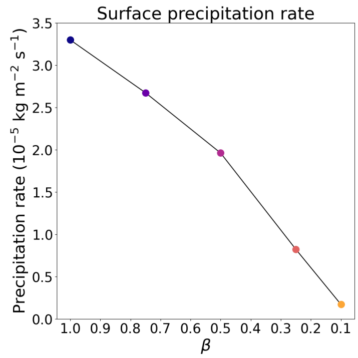

FIG. 8. Time- and horizontal-mean precipitation rate, computed during the 20-day steady-state periods from each simulation, versus β.

kg kg^{-1}—is approximately constant as β varies[4]. This implies that the relative humidity near the convective top does not strongly vary under surface drying, which is confirmed by inspection of the isentropic-average relative humidity (calculated as in Régibeau-Rockett et al. (2024)) for the different simulations shown in Fig. 9.

Similarly, comparison of the deep trajectories in Fig. 5b,f reveals that although under surface drying the atmospheric circulation becomes shallower in terms of its maximum height, the range of temperatures experienced by the circulation remains very steady as β lowers. This is consistent with a decrease in the tropopause height in the simulations with drier atmospheres, which is confirmed to occur by inspection of the mean vertical profiles of temperature in the simulations (Fig. 6). Note that the range of temperatures sampled by the deep trajectories is not constant with height in our two PBL scheme sensitivity tests (Text S3), as will be elaborated in the next section.

4. Discussion

In this work, we have investigated the changing characteristics of moist convection subjected to surface drying from the thermodynamic perspective of the convective isentropic streamfunction. Our findings are as follows: as the surface dries, the separation in the entropy of convective updraft air and downwelling air decreases (Fig. 2). This is accompanied by an increase in the convective mass transport and a deepening of the PBL (Figs. 2, 3 and 5f). Meanwhile, the total heating and cooling of the atmosphere, represented by the surface total heat fluxes and domain-integrated net radiative cooling, decrease as the parameter β decreases (Fig. 4). In RCE, the differential

[4]This result is replicated for our simulations with NSSL microphysics, but not for those with Thompson microphysics (Text S2).

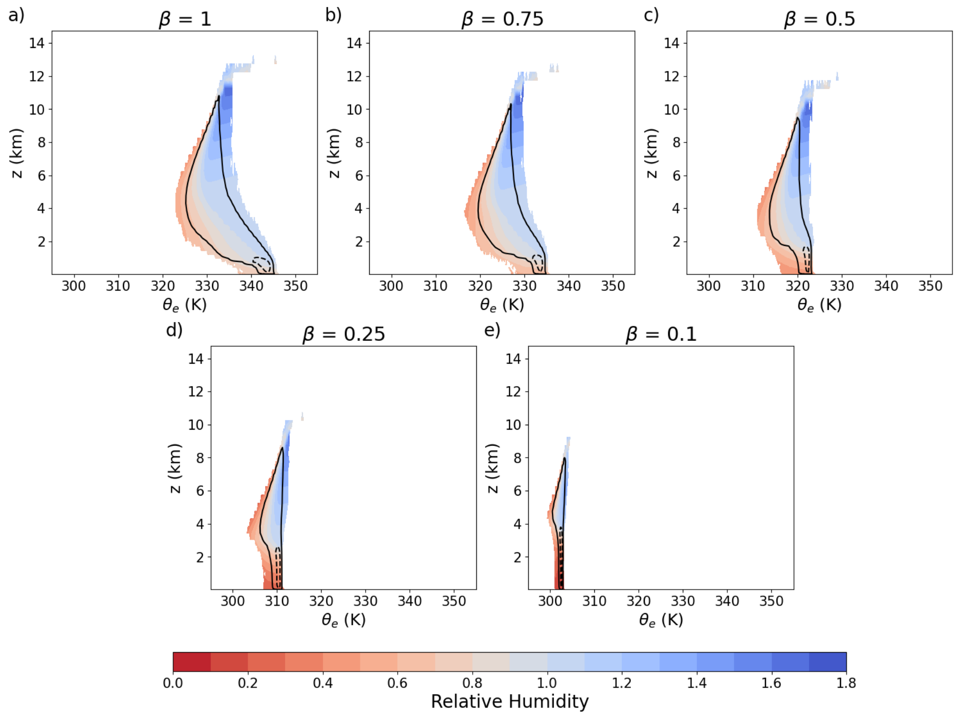

FIG. 9. Comparison of the mass-weighted isentropic-average relative humidity $\tilde{\mathscr{H}}$ (colors), and the deepest and median trajectories from ψ for the simulations with $\beta =$ a) 1, b) 0.75, c) 0.5, d) 0.25, and e) 0.1. All quantities are computed during the 20-day steady-state periods from each simulation.

atmospheric heating resulting from the combined actions of radiative cooling and the surface heat fluxes is balanced by convective heat transport. This implies that the heat transport by convection must also decrease as β reduces. The convective heat transport is dependent on both the mass transport by convection and the difference in equivalent potential temperature between the updraft and downdraft. Although the convective mass transport increases in response to drier conditions, this does not contradict the inferred decrease in the convective heat transport because there is a strong reduction in the updraft/downdraft equivalent potential temperature difference under surface drying.

Further insight into the response of convection to surface drying is gained by projecting the isentropic streamfunction into various thermodynamic spaces (Fig. 5), such as temperature-entropy space (Fig. 5a,b). The weakening gradient of entropy along the updraft of the deepest trajectories in the isentropic streamfunction in the drier simulations is indicative of lessening exchange of water mass with the environment due to entrainment and detrainment. This is likely a result of the decreasing gradient of water vapor between the updraft and its surroundings rather than reflecting decreased entrainment and detrainment. We additionally find that for the deepest convective trajectories, the temperature difference between the surface and the top of the circulation is insensitive to surface drying, although this result is not robust to the choice of PBL parameterization. Combined with the lowering height of the tropopause, this results in the atmosphere containing shallower convection in our drier simulations. Other findings of this work include that surface drying results in a reduced precipitation rate, greater irreversibility associated with surface evaporation, and a reduction in the temperature of the LCL.

The growth in the convective mass transport that we observe as the surface dries is in line with the findings of previous CPM studies of disorganized RCE convection (Pauluis 2000; Pauluis and Held 2002a; Singh and O'Neill 2022). Pauluis and Held (2002a) and Singh and O'Neill (2022) compare moist and dry RCE simulations, finding that convective updrafts are more ubiquitous in their model domains in dry RCE compared to moist RCE. This could correspond to a larger overall convective mass transport. Pauluis and Held (2002a) additionally find that the turbulent dissipation of kinetic energy—which in a steady state is equal to the rate of kinetic energy work associated with convective motions—is much larger in dry RCE than in moist RCE. This metric is strongly related to the mass transport by convection, and so this finding is in agreement with the larger convective mass transport that we find in our drier simulations. However, our findings are qualitatively different from those of three previous studies investigating the impacts of atmospheric drying on tropical cyclones specifically: first, Alland et al. (2017) finds that the convective mass transport by the TC eyewall updraft decreases as the initial amount of moisture above the LCL decreases over their suite of simulation ensembles. Meanwhile, Mrowiec et al. (2011) and Cronin and Chavas (2019) both observe decreases in the eyewall updraft velocity in dry tropical cyclones compared to moist simulations of these storms. The contrast between the response of TC updrafts and localized convective updrafts to atmospheric drying may represent a difference in the response of tropical cyclones, which are highly organized convective systems, to changes in atmospheric moisture compared to the response of disorganized convection. It is possible that the behavior of other organized convective systems, such as mesoscale convective systems or extratropical cyclones, may follow more closely the response of tropical cyclones to surface drying than the changing behavior of disorganized convection that we observe here. A study comparing the impacts of surface drying on organized convective systems to the response of disorganized convection to the same change has not been attempted to date.

The increase in the convective mass transport occurs despite a reduction in the total convective heat transport implied by the decreases we observe in the total surface heat flux and net radiative cooling at lower β values. A decrease in the total surface heat flux was observed in dry RCE compared to moist RCE by both Pauluis and Held (2002a) and Singh and O'Neill (2022). Wang and Lin (2021) also found that dry TCs experience less radiative cooling than moist TCs. Pauluis (2000) investigated these changes in greater detail and observed a gradual decrease in the net radiative heat loss of the atmosphere over a suite of RCE simulations spanning from fully moist to fully dry conditions, although it should be noted that the author employed a simpler Newtonian cooling scheme for radiation compared to our fully interactive radiative scheme.

In our experiments, surface drying results in a deepening of the PBL. This increase in the boundary layer depth is in line with results of previous observational studies, which generally find that the daily-maximum height of the PBL is largest over drier regions, such as Australia, the Sahara, and the western United States (Seidel et al. 2012; von Engeln and Teixeira 2013; Zhang et al. 2020). This result is additionally consistent with the study of Wang and Lin (2020), who find that dry TCs have a deeper inflow layer compared to moist TCs. Because TC inflow occurs in the TC boundary layer, this implies that this layer was deeper in their dry experiment than under moist conditions. Zsom et al. (2012)'s 1D cloud model study also presents results consistent with ours. For an Earth-like configuration of their model, the authors observe that lower atmospheric relative humidity causes liquid water clouds to form at higher elevations, implying a deeper PBL. The deepening of the PBL under surface drying in our simulations is due to the increase in height of the LCL. The height of the LCL is set by a combination of two factors: the atmospheric vertical lapse rate and the temperature of the LCL itself, where the latter is a result of the surface dryness combined with the temperature-dependent constraint on the mass fraction of atmospheric water vapor (Bolton 1980). Below the LCL, the lapse rate is invariant with surface drying (Fig. 6), which is to be expected due to the lack of latent heat release below the LCL. At the same time, the surface drying itself acts to increase the height of the LCL via decreasing its temperature. Overall, this results in a higher LCL for the lower-β simulations. A similar explanation is briefly provided by Seidel et al. (2012) to explain the deeper PBLs they identify in the drier U.S. compared to Europe.

We also find that the simulations with lower β values have lower tropopause heights (Fig. 6). Cronin and Chavas (2019) find an increase of the pressure of the tropopause with surface drying in their moist-to-dry simulations, although this does not necessarily imply a decrease in the tropopause height. A lower tropopause height in dry compared to moist RCE was observed by Singh and O'Neill (2022) in their simulations of localized convection. Specifically, the authors find that the tropopause is roughly 5 km lower in their dry simulation compared to the moist simulation. Assuming a linear scaling of the tropopause height with surface drying, this would correspond to a decrease of 4.5 km from fully moist conditions to those corresponding to our simulation with $\beta = 0.1$. In comparison, the height of the lapse-rate tropopause (WMO 1957) in our simulations, computed as in Xian and Homeyer (2019), decreases by 2.5 km between the fully moist and driest simulations (not shown). This is substantially less than the estimated decrease given the results of Singh and O'Neill (2022). This may indicate that the majority of the transition towards a fully dry temperature lapse rate—and an associated decrease in the tropopause—chiefly occurs at low values of atmospheric moisture below the range studied here. It is also possible that this results from the differences in the construction of Singh and O'Neill (2022)'s moist and dry simulations compared to our surface relative humidity scaling. Finally, we note that Pauluis (2000) does not observe a consistently-signed change in the height of the tropopause with atmospheric drying: for experiments in which the whole atmosphere's specific humidity is reduced to 50% and 5% of its fully moist value, respectively, the tropopause height decreases as the atmosphere dries, in line with our results. However, when the specific humidity is further reduced from 5% to 0.5% of its fully moist value, the tropopause height increases as the atmosphere becomes drier. The lowest value of β examined in our simulations is above the range at which Pauluis (2000) observes a reversal in the tropopause height's response to surface drying. It is possible that we would find non-monotonicity in our simulations if we examined lower β values.

The deepening PBL combined with the lower tropopause result in much shallower atmospheric convection in our drier experiments. This is consistent with the shallower convection found in dry RCE compared to moist RCE by Pauluis and Held (2002a) and Singh and O'Neill (2022). Mrowiec et al. (2011) and Cronin and Chavas (2019) also find that the overturning circulation of their simulated tropical cyclones is shallower in dry or near-dry RCE than in moist RCE.

Finally, a projection of the isentropic streamfunction into temperature-entropy space reveals that for the deepest convective trajectories, the temperature difference between the surface and convective tops is largely insensitive to changes in the surface moisture. The surface temperature was constant across our simulations, so this invariance is equivalent to a lack of variation in the minimum temperature achieved by the deepest convective trajectories with surface drying. Because the minimum temperature of convective clouds typically occurs at the cloud top, this implies that the cloud top temperature is approximately constant with varying surface moisture in our simulations. Hartmann and Larson (2002) introduced the Fixed Anvil Temperature (FAT) hypothesis, which argues that the temperature of tropical cloud anvils remains fixed regardless of the surface temperature. Although some studies have challenged the existence of FAT and proposed alternatives (e.g. Zelinka and Hartmann 2010; Igel et al. 2014; Seeley et al. 2019), several numerical modeling and observational studies have supported FAT (e.g. Xu et al. 2005; Kuang and Hartmann 2007; Eitzen et al. 2009; Khairoutdinov and Emanuel 2013; Singh and O'Gorman 2015), and the hypothesis has been extended from the context of the tropics to the global atmosphere (Thompson et al. 2017). Although the FAT hypothesis was developed for the context of an atmosphere under an increasing surface temperature, its arguments may be applicable to cloud anvil temperature variability under varying surface moisture. This is because the main arguments of FAT are based on the following (Hartmann and Larson 2002):

- The Clausius-Clapeyron relation places a temperature-dependent constraint on atmospheric moisture content.
- Clear-sky radiative cooling in the troposphere is dominated by longwave emission from water vapor.
- A maximum decrease of clear-sky radiative cooling with height (occurring at around the level where the atmospheric water vapor content becomes negligible, assuming the first and second listed points are valid) creates a maximum in clear-sky convergence, which must be balanced by strong convective divergence.

The first and third statements above should hold true regardless of the total amount of moisture at the surface and in the atmosphere itself. The second argument may not be valid in an atmosphere with sufficiently low water vapor, or in one in which constituents other than water vapor make major contributions to radiative cooling. However, for an atmosphere without such alternative emitters the constancy of the lowest temperature experienced by convection across our simulations implies that the FAT hypothesis can be applied to the atmosphere over different levels of surface moisture. This is somewhat consistent with the results of Thuburn and Craig (2002), who find in a simple radiative-convective model without explicit convection that the temperature of the convective top is approximately constant with decreasing atmospheric relative humidity down to a relative humidity of 40%, beyond which the convective top temperature grows with decreasing relative humidity.

Although the main results presented here imply that the temperature of convective tops may be constant as the surface dries, this result is not robust to the choice of PBL scheme (Text S3). Indeed, in both of the PBL sensitivity simulations, the lowest temperature sampled by the deep trajectories increased by roughly 7-8 K from the fully moist to the driest simulations (not shown). This is qualitatively in line with the increase in the temperature of convective tops found by Thuburn and Craig (2002) over the atmospheric moist to dry transition, although our sensitivity experiments do not support their finding that the convective-top temperature is invariant for higher values of atmospheric moisture content ($\beta \geq 0.5$) (Text S3). Prior studies employing both the YSU and MYNN PBL parameterizations have largely found support for FAT under varying surface temperatures (Satoh et al. 2012; Tsushima et al. 2014; Cesana et al. 2017; Ohno and Satoh 2018; Núñez Ocasio and Dougherty 2024), implying that validation of this hypothesis is not dependent on the choice of PBL scheme. An extension of FAT to the context of varying surface moisture has not previously been investigated, and taken together our results are inconclusive regarding whether such an extension is valid. Future studies should use methods other than isentropic analysis to investigate whether the FAT hypothesis might be extended to situations besides varying surface temperature, such as varying surface moisture.

This work includes several idealizations that may limit the applicability of our findings to real atmospheric convection. First, our simulations are conducted over an oceanic lower boundary. Although the drying of this lower boundary may still capture some of the convective changes resulting from atmospheric drying over land, there are many important differences between land and ocean lower boundary conditions, even in highly idealized models. Future work should verify whether the convective changes in response to atmosphere drying that we see here are generalizable to atmospheres over land. Second, the behavior of convection in response to atmospheric drying discussed here may depend on the surface layer parameterization employed in our study. Future work should verify whether our results are robust under alternative surface schemes. Finally, the simulations analyzed here are designed based on the characteristics of Earth's current atmosphere. Although it is possible that our findings could be generalized to the atmospheres of other planets with significant atmospheric water vapor, ensuing studies should verify whether our findings hold true when the similarity of the simulated atmosphere to Earth's is relaxed.

Acknowledgments. We are grateful to Olivier Pauluis, Noah Diffenbaugh, Leif Thomas, and Aditi Sheshadri for their helpful feedback on this manuscript. We are also thankful to the Stanford Research Computing Center staff for their technical support during this project, and for allowing us to carry out this study via the use of their high-performance computing cluster. We are additionally grateful to George Bryan for creating and maintaining the CM1 model code for the community. Some portions of this paper are published in thesis form in fulfillment of the requirements for the Ph.D. (Régibeau-Rockett 2025).

Data availability statement. All simulations were run using the Cloud Model 1, version 21.1, which is available at `https://www2.mmm.ucar.edu/people/bryan/cm1/`. Modified model source code, as well as input and output files, is available at `https://doi.org/10.5281/zenodo.17352677`. Finally, our analysis code is located at `https://doi.org/10.5281/zenodo.17352688`.

APPENDIX

Computation of the energy budget

In a simulated RCE atmosphere, the total energy of the atmosphere is statistically steady and conservation of energy requires that:

$$\overline{LHF} + \overline{SHF} + [Q_{rad}] = 0, \tag{A1}$$

where $\overline{X}$ denotes the time- and horizontal-mean value of X, and $[X]$ is equal to the time-average, domain-integrated value of X divided by the area of the surface. The terms LHF and SHF (W m^{-2}) are the bulk surface fluxes of latent and sensible heat, repectively, and Q_{rad} (W m^{-3}) is the radiative heating rate per unit volume. The LHF is defined as in Eq. (1), and the SHF is computed in the model as (Jiménez et al. 2012):

$$SHF = \rho_1 c_{p,d} C_h U (\theta_s - \theta_1).$$

Here, $c_{p,d}$ (J kg^{-1} K^{-1}) is the specific heat capacity of dry air at constant pressure, C_h is a dimensionless bulk transfer coefficient, and θ_s and θ_1 are, respectively, the potential temperature (K) at the surface and at the lowest model level.

The first law of thermodynamics under moist, constant-volume conditions states that:

$$dQ = \rho c_{v,m} dT, \tag{A2}$$

where ρ (kg m^{-3}) is the dry-air density and $c_{v,m}$ (J kg^{-1} K^{-1}) is the heat capacity of humid air under constant-volume conditions, defined as in CM1:

$$c_{v,m} = c_{v,d} + c_{v,v} r_v + c_{p,l} r_l + c_{p,fr} r_{fr}.$$

Here, $c_{v,d}$ (J kg^{-1} K^{-1}) is the heat capacity of dry air under constant-volume conditions, $c_{v,v}$ (J kg^{-1} K^{-1}) is the heat capacity at constant volume of water vapor, and $c_{p,l}$ and $c_{p,fr}$ are the heat capacities of liquid and solid water under constant-pressure conditions (J kg^{-1} K^{-1}). The terms r_v, r_l, and r_{fr} are the mixing ratios of water vapor, liquid water, and solid water (kg kg^{-1}).

In accordance with Eq. (A2), Q_{rad} is computed from the model-output time tendencies of temperature due to the longwave and shortwave forcings in the radiative scheme, $\dot{T}_{rad,SW}$ and $\dot{T}_{rad,LW}$, as:

$$Q_{rad} = \rho c_{v,m} (\dot{T}_{rad,SW} + \dot{T}_{rad,LW}). \tag{A3}$$

References

Alland, J. J., B. H. Tang, and K. L. Corboseiro, 2017: Effects of Midlevel Dry Air on Development of the Axisymmetric Tropical Cyclone Secondary Circulation. *J. Atmos. Sci.*, **74**, 1455–1470, https://doi.org/10.1175/JAS-D-16-0271.1.

Barth, E. L., and S. C. R. Rafkin, 2007: TRAMS: A new dynamic cloud model for Titan's methane clouds. *Geophys. Res. Lett.*, **34**, L03 203, https://doi.org/10.1029/2006GL028652.

Beljaars, A. C. M., 1995: The parametrization of surface fluxes in large-scale models under free convection. *Quart. J. Roy. Meteor. Soc.*, **121**, 255–270, https://doi.org/10.1002/qj.49712152203.

Benneke, B., and Coauthors, 2019: Water Vapor and Clouds on the Habitable-zone Sub-Neptune Exoplanet K2-18b. *The Astrophysical Journal Letters*, **887**, L14, https://doi.org/10.3847/2041-8213/ab59dc.

Benneke, B., and Coauthors, 2024: JWST Reveals CH4, CO2, and H2O in a Metal-rich Miscible Atmosphere on a Two-Earth-Radius Exoplanet. *arXiv astro-ph.EP 2403.03325 [Preprint]*, URL https://arxiv.org/abs/2403.03325.

Bolton, D., 1980: The Computation of Equivalent Potential Temperature. *Mon. Wea. Rev.*, **108**, 1046–1053, https://doi.org/10.1175/1520-0493(1980)108⟨1046:TCOEPT⟩2.0.CO;2.

Bretherton, C. S., P. N. Blossey, and M. Khairoutdinov, 2005: An Energy-Balance Analysis of Deep Convective Self-Aggregation above Uniform SST. *J. Atmos. Sci.*, **62**, 4273–4292, https://doi.org/10.1175/JAS3614.1.

Bryan, G. H., 2008: On the Computation of Pseudoadiabatic Entropy and Equivalent Potential Temperature. *Mon. Wea. Rev.*, **136**, 5239–5245, https://doi.org/10.1175/2008MWR2593.1.

Bryan, G. H., and J. M. Fritsch, 2002: A Benchmark Simulation for Moist Nonhydrostatic Numerical Models. *Mon. Wea. Rev.*, **130**, 2917–2928, https://doi.org/10.1175/1520-0493(2002)130⟨2917:ABSFMN⟩2.0.CO;2.

Bryan, G. H., and R. Rotunno, 2009: The Maximum Intensity of Tropical Cyclones in Axisymmetric Numerical Model Simulations. *Mon. Wea. Rev.*, **137**, 1770–1789, https://doi.org/10.1175/2008MWR2709.1.

Cadieux, C., and Coauthors, 2022: TOI-1452 b: SPIRou and TESS Reveal a Super-Earth in a Temperate Orbit Transiting an M4 Dwarf. *The Astrophysical Journal*, **164**, 96, https://doi.org/10.3847/1538-3881/ac7cea.

Cadieux, C., and Coauthors, 2024: New Mass and Radius Constraints on the LHS 1140 planets: LHS 1140 b Is either a Temperate Mini-Neptune or a Water World. *The Astrophysical Journal Letters*, **960**, L3, https://doi.org/10.3847/2041-8213/ad1691.

Cesana, G., K. Suselj, and F. Brient, 2017: On the dependence of cloud feedbacks on physical parameterizations in WRF aquaplanet simulations. *Geophys. Res. Lett.*, **44**, 10 762–10 771, https://doi.org/10.1002/2017GL074820.

Changeat, Q., B. Edwards, A. F. Al-Refaie, A. Tsiaras, I. P. Waldmann, and G. Tinetti, 2019: Disentangling atmospheric compositions of K2-18 b with next generation facilities. *Exp. Astron.*, **53**, 391–416, https://doi.org/10.1007/s10686-021-09794-w.

Cronin, T. W., and D. R. Chavas, 2019: Dry and Semidry Tropical Cyclones. *J. Atmos. Sci.*, **76**, 2193–2212, https://doi.org/10.1175/JAS-D-18-0357.1.

Dauhut, T., J.-P. Chaboureau, P. Mascart, and O. Pauluis, 2017: The Atmospheric Overturning Induced by Hector the Convector. *J. Atmos. Sci.*, **74**, 3271–3284, https://doi.org/10.1175/JAS-D-17-0035.1.

Ding, F., and R. T. Pierrehumbert, 2016: Convection in Condensible-Rich Atmospheres. *The Astrophysical Journal*, **822**, 24, https://doi.org/10.3847/0004-637X/822/1/24.

Dunion, J. P., 2011: Rewriting the Climatology of the Tropical North Atlantic and Caribbean Sea Atmosphere. *J. Climate*, **24**, 893–908, https://doi.org/10.1175/2010JCLI3496.1.

Eitzen, Z. A., K. Xu, and T. Wong, 2009: Cloud and Radiative Characteristics of Tropical Deep Convective Systems in Extended Cloud Objects from CERES Observations. *J. Climate*, **22**, 5983–6000, https://doi.org/10.1175/2009JCLI3038.1.

Emanuel, K. A., and M. Bister, 1996: Moist convective velocity and buoyancy scales. *J. Atmos. Sci.*, **53**, 3276–3285, https://doi.org/10.1175/1520-0469(1996)053⟨3276:MCVABS⟩2.0.CO;2.

Evans, D. A., N. J. Beukes, and J. L. Kirschvink, 1997: Low-latitude glaciation in the Palaeoproterozoic era. *Nature*, **386**, 262–266, https://doi.org/10.1038/386262a0.

Fang, J., O. Pauluis, and F. Zhang, 2019: The Thermodynamic Cycles and Associated Energetics of Hurricane Edouard (2014) during Its Intensification. *J. Atmos. Sci.*, **76**, 1769–1784, https://doi.org/10.1175/JAS-D-18-0221.1.

Grell, G. A., J. Dudhia, and D. R. Stauffer, 1994: A description of the fifth-generation Penn State/NCAR Mesoscale Model (MM5). Tech. rep., NCAR Tech. Note NCAR TN-398-1-STR.

Hartmann, D. L., and K. Larson, 2002: An important constraint on tropical cloud - climate feedback. *Geophys. Res. Lett.*, **29**, 1951, https://doi.org/10.1029/2002GL015835.

Hoffman, P. F., A. J. Kaufman, G. P. Halverson, and D. P. Schrag, 1998: A Neoproterozoic Snowball Earth. *Science*, **281**, 1342–1346, https://doi.org/10.1126/science.281.5381.1342.

Hong, S.-Y., Y. Noh, and J. Dudhia, 2006: A New Vertical Diffusion Package with an Explicit Treatment of Entrainment Processes. *Mon. Wea. Rev.*, **134**, 2318–2341, https://doi.org/10.1175/MWR3199.1.

Hong, S.-Y., and H. Pan, 1996: Nonlocal Boundary Layer Vertical Diffusion in a Medium-Range Forecast Model. *Mon. Wea. Rev.*, **124**, 2322–2339, https://doi.org/10.1175/1520-0493(1996)124⟨2322:NBLVDI⟩2.0.CO;2.

Hueso, R., and A. Sánchez-Lavega, 2006: Methane storms on Saturn's moon Titan. *Nature*, **442**, 428–431, https://doi.org/10.1038/nature04933.

Igel, M. R., A. J. Drager, and S. C. van den Heever, 2014: A CloudSat cloud object partitioning technique and assessment and integration of deep convective anvil sensitivities to sea surface temperature. *J. Geophys. Res. Atmos.*, **119**, 10 515–10 535, https://doi.org/10.1002/2014JD021717.

Jeevanjee, N., and D. M. Romps, 2013: Convective self-aggregation, cold pools, and domain size. *Geophys. Res. Lett.*, **40**, 994–998, https://doi.org/10.1002/grl.50204.

Jiménez, P. A., J. Dudhia, J. F. González-Rouco, J. Navarro, J. P. Montávez, and E. García-Bustamante, 2012: A Revised Scheme for the WRF Surface Layer Formulation. *Mon. Wea. Rev.*, **140**, 898–918, https://doi.org/10.1175/MWR-D-11-00056.1.

Kasting, J. F., 1988: Runaway and moist greenhouse atmospheres and the evolution of Earth and Venus. *Icarus*, **74**, 472–494, https://doi.org/10.1016/0019-1035(88)90116-9.

Khairoutdinov, M. F., and K. A. Emanuel, 2013: Rotating radiative-convective equilibrium simulated by a cloud-resolving model. *Journal of Advances in Modeling Earth Systems*, **5**, 816–825, https://doi.org/10.1002/2013MS000253.

Kirschvink, J. L., 1992: *Late Proterozoic low-latitude global glaciation: the snowball Earth. In: The Proterozoic biosphere: A multidisciplinary study [Schopf, J. and C. Klein (eds.)]*, 51–52. Cambridge University Press, Cambridge, United Kingdom and New York, NY, USA, https://doi.org/10.1017/CBO9780511601064.

Kuang, Z., and D. L. Hartmann, 2007: Testing the Fixed Anvil Temperature Hypothesis in a Cloud-Resolving Model. *J. Climate*, **20**, 2051–2057, https://doi.org/10.1175/JCLI4124.1.

Li, C., and A. Ingersoll, 2015: Moist convection in hydrogen atmospheres and the frequency of Saturn's giant storms. *Nature Geosci.*, **8**, 398–403, https://doi.org/10.1038/ngeo2405.

Li, Y., Y. Wang, and Z.-M. Tan, 2023: Is the outflow-layer inertial stability crucial to the energy cycle and development of tropical cyclones? *J. Atmos. Sci.*, https://doi.org/10.1175/JAS-D-22-0186.1.

Madhusudhan, N., M. C. Nixon, L. Welbanks, A. A. A. Piette, and R. A. Booth, 2020: The Interior and Atmosphere of the Habitable-zone Exoplanet K2-18b. *The Astrophysical Journal Letters*, **891**, L7, https://doi.org/10.3847/2041-8213/ab7229.

Mahrt, L. T., and J. Sun, 1995: The subgrid velocity scale in the bulk aerodynamic relationship for spatially averaged scalar fluxes. *Mon. Wea. Rev.*, **123**, 3032–3041, https://doi.org/10.1175/1520-0493(1995)123⟨3032:TSVSIT⟩2.0.CO;2.

Mansell, E., and C. L. Ziegler, 2010: Aerosol Effects on Simulated Storm Electrification and Precipitation in a Two-Moment Bulk Microphysics Model. *J. Atmos. Sci.*, **70**, 2032–2050, https://doi.org/10.1175/JAS-D-12-0264.1.

Mansell, E., C. L. Ziegler, and E. C. Bruning, 2010: Simulated Electrification of a Small Thunderstorm with Two-Moment Bulk Microphysics. *J. Atmos. Sci.*, **67**, 171–194, https://doi.org/10.1175/2009JAS2965.1.

Marquet, P., 2011: Definition of a moist entropy potential temperature: application to FIRE-I data flights. *Quart. J. Roy. Meteor. Soc.*, **137**, 768–791, https://doi.org/10.1002/qj.787.

Marquet, P., 2017: A third-law isentropic analysis of a simulated hurricane. *J. Atmos. Sci.*, **74**, 3451–3471, https://doi.org/10.1175/JAS-D-17-0126.1.

Mikal-Evans, T., N. Madhusudhan, J. Dittmann, M. N. Günther, L. Welbanks, V. V. Eylen, I. J. M. C. T. Daylan, and L. Kreidberg, 2023: Hubble Space Telescope Transmission Spectroscopy for the Temperate Sub-Neptune TOI-270 d: A Possible Hydrogen-rich Atmosphere Containing Water Vapor. *The Astronomical Journal*, **165**, 84, https://doi.org/10.3847/1538-3881/aca90b.

Mitchell, J., 2008: The drying of Titan's dunes: Titan's methane hydrology and its impact on atmospheric circulation. *J. Geophys. Res.*, **113**, E08 015, https://doi.org/10.1029/2007JE003017.

Mitchell, J., and J. M. Lora, 2016: The Climate of Titan. *Annual Review of Earth and Planetary Sciences*, **44**, 353–380, https://doi.org/10.1146/annurev-earth-060115-012428.

Mitchell, J., R. Pierrehumbert, D. Frierson, and R. Caballero, 2006: The dynamics behind Titan's methane clouds. *Proc. Natl. Acad. Sci. (USA)*, **103**, 18 421–18 426, https://doi.org/10.1073/pnas.0605074103.

Morrison, H., J. A. Curry, and V. I. Khvorostyanov, 2005: A New Double-Moment Microphysics Parameterization for Application in Cloud and Climate Models. Part I: Description. *J. Atmos. Sci.*, **62**, 1665–1677, https://doi.org/10.1175/JAS3446.1.

Morrison, H., G. Thompson, and V. Tatarskii, 2009: Impact of Cloud Microphysics on the Development of Trailing Stratiform Precipitation in a Simulated Squall Line: Comparison of One- and Two-Moment Schemes. *Mon. Wea. Rev.*, **137**, 991–1007, https://doi.org/10.1175/2008MWR2556.1.

Mrowiec, A. A., S. T. Garner, and O. M. Pauluis, 2011: Axisymmetric Hurricane in a Dry Atmosphere: Theoretical Framework and Numerical Experiments. *J. Atmos. Sci.*, **68**, 1607–1619, https://doi.org/10.1175/2011JAS3639.1.

Mrowiec, A. A., O. M. Pauluis, A. M. Frindlind, and A. S. Ackerman, 2015: Properties of a Mesoscale Convective System in the Context of an Isentropic Analysis. *J. Atmos. Sci.*, **72**, 1945–1962, https://doi.org/10.1175/JAS-D-14-0139.1.

Mrowiec, A. A., O. M. Pauluis, and F. Zhang, 2016: Isentropic Analysis of a Simulated Hurricane. *J. Atmos. Sci.*, **73**, 1857–1870, https://doi.org/10.1175/JAS-D-15-0063.1.

Muller, C. J., and I. M. Held, 2012: Detailed Investigation of the Self-Aggregation of Convection in Cloud-Resolving Simulations. *J. Atmos. Sci.*, **69**, 2551–2565, https://doi.org/10.1175/JAS-D-11-0257.1.

Muller, C. J., and D. M. Romps, 2018: Acceleration of tropical cyclogenesis by self-aggregation feedbacks. *Proc. Natl. Acad. Sci. (USA)*, **115**, 2930–2935, https://doi.org/10.1073/pnas.1719967115.

Nakanishi, M., and H. Niino, 2006: An Improved Mellor–Yamada Level-3 Model: Its Numerical Stability and Application to a Regional Prediction of Advection Fog. *Boundary-Layer Meteorol.*, **119**, 397–407, https://doi.org/10.1007/s10546-005-9030-8.

Nakanishi, M., and H. Niino, 2009: Development of an Improved Turbulence Closure Model for the Atmospheric Boundary Layer. *J. Meteor. Soc. Japan*, **87**, 895–912, https://doi.org/10.2151/jmsj.87.895.

Núñez Ocasio, K. M., and E. M. Dougherty, 2024: The effect of pseudo-global warming on the weather-climate system of Africa in a convection-permitting model. *Geophys. Res. Lett.*, **51**, e2024GL112 341, https://doi.org/10.1029/2024GL112341.

Ohno, T., and M. Satoh, 2018: Roles of cloud microphysics on cloud responses to sea surface temperatures in radiative-convective equilibrium experiments using a high-resolution global nonhydrostatic model. *J. Adv. Model. Earth Syst.*, **10**, 1970–1989, https://doi.org/10.1029/2018MS001386.

Olson, J. B., J. S. Kenyon, W. M. Angevine, J. M. . Brown, M. Pagowski, and K. Sušelj, 2019: A Description of the MYNN-EDMF Scheme and the Coupling to Other Components in WRF–ARW. *NOAA Technical Memorandum OAR GSD*, **61**, 37, https://doi.org/10.25923/n9wm-be49.

O'Neill, M., and D. R. Chavas, 2020: Inertial Waves in Axisymmetric Tropical Cyclones. *J. Atmos. Sci.*, **77**, 2501–2517, https://doi.org/10.1175/JAS-D-19-0330.1.

Pauluis, O., and I. M. Held, 2002a: Entropy Budget of an Atmosphere in Radiative–Convective Equilibrium. Part I: Maximum Work and Frictional Dissipation. *J. Atmos. Sci.*, **59**, 125–139, https://doi.org/10.1175/1520-0469(2002)059⟨0125:EBOAAI⟩2.0.CO;2.

Pauluis, O., and I. M. Held, 2002b: Entropy Budget of an Atmosphere in Radiative–Convective Equilibrium. Part II: Latent Heat Transport and Moist Processes. *J. Atmos. Sci.*, **59**, 140–149, https://doi.org/10.1175/1520-0469(2002)059⟨0140:EBOAAI⟩2.0.CO;2.

Pauluis, O. M., 2000: Entropy budget of an atmosphere in radiative–convective equilibrium. Ph.D. thesis, Princeton University.

Pauluis, O. M., 2011: Water Vapor and Mechanical Work: A Comparison of Carnot and Steam Cycles. *J. Atmos. Sci.*, **68**, 91–102, https://doi.org/10.1175/2010JAS3530.1.

Pauluis, O. M., 2016: The Mean Air Flow as Lagrangian Dynamics Approximation and Its Application to Moist Convection. *J. Atmos. Sci.*, **73**, 4407–4425, https://doi.org/10.1175/JAS-D-15-0284.1.

Pauluis, O. M., and A. A. Mrowiec, 2013: Isentropic Analysis of Convective Motions. *J. Atmos. Sci.*, **70**, 3673–3688, https://doi.org/10.1175/JAS-D-12-0205.1.

Pauluis, O. M., and F. Zhang, 2017: Reconstruction of Thermodynamic Cycles in a High-Resolution Simulation of a Hurricane. *J. Atmos. Sci.*, **74**, 3367–3381, https://doi.org/10.1175/JAS-D-16-0353.1.

Piaulet, C., and Coauthors, 2023: Evidence for the volatile-rich composition of a 1.5-Earth-radius planet. *Nat. Astron.*, **7**, 206–222, https://doi.org/10.1038/s41550-022-01835-4.

Piaulet-Ghorayeb, C., and Coauthors, 2024: JWST/NIRISS Reveals the Water-rich ”Steam World” Atmosphere of GJ 9827 d. *The Astrophysical Journal Letters*, **974**, L10, https://doi.org/10.3847/2041-8213/ad6f00.

Pierrehumbert, R. T., and F. Ding, 2016: Dynamics of atmospheres with a non-dilute condensible component. *Proc. Roy. Soc. A: Mathematical, Physical and Engineering Sciences*, **472**, 20160 107, https://doi.org/10.1098/rspa.2016.0107.

Régibeau-Rockett, L., 2025: Thermodynamic behavior of atmospheric heat engines in different environments. Ph.D. thesis, Stanford University.

Régibeau-Rockett, L., O. M. Pauluis, and M. E. O'Neill, 2024: Investigating the Relationship between Sea Surface Temperature and the Mechanical Efficiency of Tropical Cyclones. *J. Climate*, **37**, 439–456, https://doi.org/10.1175/JCLI-D-22-0877.1.

Rennó, N. O., and A. P. Ingersoll, 1996: Natural convection as a heat engine: A theory for CAPE. *J. Atmos. Sci.*, **53**, 572–585, https://doi.org/10.1175/1520-0469(1996)053⟨0572:NCAAHE⟩2.0.CO;2.

Roy, P.-A., and Coauthors, 2023: Water Absorption in the Transmission Spectrum of the Water World Candidate GJ 9827 d. *The Astrophysical Journal Letters*, **954**, L52, https://doi.org/10.3847/2041-8213/acebf0.

Satoh, M., S. Iga, H. Tomita, Y. Tsushima, and A. T. Noda, 2012: Response of Upper Clouds in Global Warming Experiments Obtained Using a Global Nonhydrostatic Model with Explicit Cloud Processes. *J. Clim.*, **25**, 2178–2191, https://doi.org/10.1175/JCLI-D-11-00152.1.

Seeley, J. T., N. Jeevanjee, and D. M. Romps, 2019: FAT or FiTT: Are anvil clouds or the tropopause temperature invariant? *Geophys. Res. Lett.*, **46**, 1842–1850, https://doi.org/10.1029/2018GL080096.

Seidel, D. J., Y. Zhang, A. Beljaars, J.-C. Golaz, A. R. Jacobson, and B. Medeiros, 2012: Climatology of the planetary boundary layer over the continental United States and Europe. *J. Geophys. Res.*, **117**, D17 106, https://doi.org/10.1029/2012JD018143.

Singh, M. S., and P. A. O'Gorman, 2015: Increases in moist-convective updraught velocities with warming in radiative-convective equilibrium. *Quart. J. Roy. Meteor. Soc.*, **141**, 2828–2838, https://doi.org/10.1002/qj.2567.

Singh, M. S., and P. A. O'Gorman, 2016: Scaling of the entropy budget with surface temperature in radiative-convective equilibrium. *Journal of Advances in Modeling Earth Systems*, **8**, 1132–1150, https://doi.org/10.1002/2016MS000673.

Singh, M. S., and M. E. O'Neill, 2022: The climate system and the second law of thermodynamics. *Rev. Mod. Phys.*, **94**, 015 001, https://doi.org/10.1103/RevModPhys.94.015001.

Skamarock, W. C., and Coauthors, 2008: A description of the advanced research WRF version 3. Tech. rep., National Center for Atmospheric Research, Boulder, Colorado, USA.

Southworth, J., L. Mancini, N. Madhusudhan, P. Mollière, S. Ciceri, and T. Henning, 2017: Detection of the Atmosphere of the 1.6 $M_\oplus$ Exoplanet GJ 1132 b. *The Astronomical Journal*, **153**, 191, https://doi.org/10.3847/1538-3881/aa6477.

Thompson, D. W. J., S. Bony, and Y. Li, 2017: Thermodynamic constraint on the depth of the global tropospheric circulation. *Proc. Natl. Acad. Sci. (USA)*, **114**, 8181–8186, https://doi.org/10.1073/pnas.1620493114.

Thompson, G., and T. Eidhammer, 2014: A Study of Aerosol Impacts on Clouds and Precipitation Development in a Large Winter Cyclone. *J. Atmos. Sci.*, **71**, 3636–3658, https://doi.org/10.1175/JAS-D-13-0305.1.

Thompson, G., P. R. Field, R. M. Rasmussen, and W. D. Hall, 2008: Explicit Forecasts of Winter Precipitation Using an Improved Bulk Microphysics Scheme. Part II: Implementation of a New Snow Parameterization. *Mon. Wea. Rev.*, **136**, 5095–5115, https://doi.org/10.1175/2008MWR2387.1.

Thuburn, J., and G. C. Craig, 2002: On the temperature structure of the tropical substratosphere. *J. Geophys. Res.*, **107**, https://doi.org/10.1029/2001JD000448.

Tsiaras, A., I. P. Waldmann, G. Tinetti, J. Tennyson, and S. N. Yurchenko, 2019: Water vapour in the atmosphere of the habitable-zone eight-Earth-mass planet K2-18 b. *Nat. Astron.*, **3**, 1086–1091, https://doi.org/10.1038/s41550-019-0878-9.

Tsushima, Y., S. Iga, H. Tomita, M. Satoh, A. T. Noda, and M. J. Webb, 2014: High cloud increase in a perturbed SST experiment with a global nonhydrostatic model including explicit convective processes. *J. Adv. Model. Earth Syst.*, **6**, 571–585, https://doi.org/10.1002/2013MS000301.

Urata, R. A., and O. B. Toon, 2013: Simulations of the martian hydrologic cycle with a general circulation model: Implications for the ancient martian climate. *Icarus*, **226**, 229–250, https://doi.org/10.1016/j.icarus.2013.05.014.

von Engeln, A., and J. Teixeira, 2013: A Planetary Boundary Layer Height Climatology Derived from ECMWF Reanalysis Data. *J. Climate*, **26**, 6575–6590, https://doi.org/10.1175/JCLI-D-12-00385.1.

Wang, D., and Y. Lin, 2020: Size and Structure of Dry and Moist Reversible Tropical Cyclones. *J. Atmos. Sci.*, **77**, 2091–2114, https://doi.org/10.1175/JAS-D-19-0229.1.

Wang, D., and Y. Lin, 2021: Potential Role of Irreversible Moist Processes in Modulating Tropical Cyclone Surface Wind Structure. *J. Atmos. Sci.*, **78**, 709–725, https://doi.org/10.1175/JAS-D-20-0192.1.

Wilhelmson, R. B., and C.-S. Chen, 1982: A Simulation of the Development of Successive Cells Along a Cold Outflow Boundary. *J. Atmos. Sci.*, **39**, 1466–1483, https://doi.org/10.1175/1520-0469(1982)039⟨1466:ASOTDO⟩2.0.CO;2.

WMO, 1957: Meteorology-A three-dimensional science: Second session of the commission for aerology. *WMO Bull.*, **4**, 134–138.

Wordsworth, R., F. Forget, E. Millour, J. W. Head, J.-B. Madeleine, and B. Charnay, 2013: Global modelling of the early martian climate under a denser CO2 atmosphere: Water cycle and ice evolution. *Icarus*, **222**, 1–19, https://doi.org/10.1016/j.icarus.2012.09.036.

Xian, T., and C. R. Homeyer, 2019: Global tropopause altitudes in radiosondes and reanalyses. *Atmos. Chem. Phys.*, **19**, 5661–5678, https://doi.org/10.5194/acp-19-5661-2019.

Xu, K., T. Wong, B. A. Wielicki, L. Parker, and Z. A. Eitzen, 2005: Statistical Analyses of Satellite Cloud Object Data from CERES. Part I: Methodology and Preliminary Results of the 1998 El Niño/2000 La Niña. *J. Climate*, **18**, 2497–2514, https://doi.org/10.1175/JCLI3418.1.

Zelinka, M. D., and D. L. Hartmann, 2010: Why is longwave cloud feedback positive? *J. Geophys. Res.*, **115**, D16 117, https://doi.org/10.1029/2010JD013817.

Zhang, Y., K. Sun, Z. Gao, Z. Pan, M. A. Shook, and D. Li, 2020: Diurnal climatology of planetary boundary layer height over the contiguous United States derived from AMDAR and reanalysis data. *J. Geophys. Res. Atmos.*, **125**, e2020JD032 803, https://doi.org/10.1029/2020JD032803.

Ziegler, C. L., 1985: Retrieval of Thermal and Microphysical Variables in Observed Convective Storms. Part 1: Model Development and Preliminary Testing. *J. Atmos. Sci.*, **42**, 1487–1509, https://doi.org/10.1175/1520-0469(1985)042⟨1487:ROTAMV⟩2.0.CO;2.

Zsom, A., L. Kaltenegger, and C. Goldblatt, 2012: A 1d microphysical cloud model for Earth, and Earth-like exoplanets: Liquid water and water ice clouds in the convective troposphere. *Icarus*, **221**, 603–616, https://doi.org/10.1016/j.icarus.2012.08.028.